

Unravelling Degradation Pathways of Oxide-Supported Pt Fuel Cell Nanocatalysts under In Situ Operating Conditions

Henrike Schmies, Arno Bergmann, Jakub Drnec, Guanxiong Wang, Detre Teschner, Stefanie Kühn, Daniel J. S. Sandbeck, Serhiy Cherevko, Martin Gocyla, Meital Shviro, Marc Heggen, Vijay Ramani, Rafal E. Dunin-Borkowski, Karl J. J. Mayrhofer, and Peter Strasser*

Knowledge of degradation pathways of catalyst/support ensembles aids the development of rational strategies to improve their stability. Here, this is exemplified using indium tin oxide (ITO)-supported Platinum nanoparticles as electrocatalysts at fuel cell (FC) cathodes under degradation protocols to mimic operating conditions in two potential regimes. The evolution of crystal structure, composition, crystallite and particle size is tracked by in situ X-ray techniques (small and wide angle scattering), metal dissolution by in situ scanning flow cell coupled with mass spectrometry (SFC ICP-MS) and Pt surface morphology by advanced electron microscopy. In a regular FC operation regime, Pt poisoning rather than Pt particle growth, agglomeration, dissolution or detachment was found to be the likely origin of the observed degradation and ORR activity losses. In the start-up regime degradation is actually suppressed and only minor losses in catalytic activity are observed. The presented data thus highlight the excellent nanoparticle stabilization and corrosion resistance of the ITO support, yet point to a degradation pathway involving Pt surface modifications by deposition of sub-monolayers of support metal ions. The identified degradation pathway of the Pt/oxide catalyst/support couple contributes to our understanding of cathode electrocatalysts for polymer electrolyte fuel cells (PEFC).

of PEFCs such as the catalyst stability at the cathode side where the oxygen reduction reaction (ORR) takes place.

Carbon supported Pt based materials are state-of-art electrocatalysts but they suffer from several degradation phenomena especially during fuel cell start-stop procedure that come along with harsh conditions (low pH, high potentials, elevated temperatures).^[1] Activity degradation mainly arises from Pt dissolution, Ostwald ripening, and/or carbon corrosion.^[2–4] Several attempts have been made to enhance the overall catalyst stability on the cathode site.^[5] For example, alloying the Pt nanoparticles with one or more transition metals like Ni not only improves the Pt mass based activity^[6] but also increases the catalyst stability.^[7] However, to completely prevent carbon corrosion alternative support materials for fuel cell catalysts were investigated in the past decade. Metal oxides have recently gained attention in this field because they

offer a variety of features required for a stable electrocatalyst for oxygen reduction.^[8] Essential properties are high surface area, high electrical conductivity, thermal stability, and above all their corrosion resistance. Therefore, several metal oxides have been investigated: Popov and co-workers showed that Pt

1. Introduction

Polymer electrolyte fuel cells (PEFCs) offer great possibilities as clean energy conversion devices. However, there are still some major issues that need to be solved for a wide commercialization

H. Schmies, Dr. A. Bergmann, Dr. S. Kühn, Prof. P. Strasser
Department of Chemistry
Chemical Engineering Division
Technical University of Berlin
10623 Berlin, Germany
E-mail: pstrasser@tu-berlin.de

Dr. J. Drnec
European Synchrotron Radiation Facility (ESRF)
38000 Grenoble, France

G. Wang, Prof. V. Ramani
School of Engineering & Applied Science
Washington University in St. Louis
63130 St. Louis, MO, USA

Dr. D. Teschner
Department of Heterogeneous Reactions
Max-Planck-Institute for Chemical Energy Conversion
45470 Mülheim an der Ruhr, 14195 Berlin, Germany

D. Teschner
Department of Inorganic Chemistry
Fritz-Haber-Institut der Max-Planck-Gesellschaft
Berlin, Germany

D. J. S. Sandbeck, Dr. S. Cherevko, Prof. K. J. J. Mayrhofer
Helmholtz-Institute Erlangen-Nürnberg for Renewable Energy (IEK-11)
Forschungszentrum Jülich, 91058 Erlangen, Germany

M. Gocyla, Dr. M. Shviro, Dr. M. Heggen, Prof. R. E. Dunin-Borkowski
Ernst-Ruska Centre for Microscopy and Spectroscopy with Electrons and
Peter Grünberg Institute
Forschungszentrum Jülich, 52425 Jülich, Germany

DOI: 10.1002/aenm.201701663

on TiO₂ has a high stability toward ORR caused by the high corrosion resistance and the strong metal support interaction (SMSI).^[9] This SMSI effect was further analyzed by Alonso-Vante and co-workers,^[10] they were able to show changes in the local electron density of Pt when deposited on titanium oxide-carbon and tungsten oxide-carbon support. By X-ray photoelectron spectroscopy (XPS) analysis they determined an increase in the asymmetry of the Pt 4f peak which the authors attributed to either an alloy formation between Pt and the support or a partial charge transfer from the support to Pt. Furthermore, a molybdenum-doped Ti dioxide was found to be a stable electrocatalyst because of electronic structure changes in the Pt upon synergistic interaction with the support material.^[11] A similar phenomenon was observed for Pt/Ta_{0.3}Ti_{0.7}O₂ where the electrochemical surface area (ECSA) decreased less compared to Pt/C reference catalyst when exposed to accelerated load cycling test designed to test the electrocatalyst stability.^[12,13] The catalyst exhibited good activity when tested in an operating fuel cell and exceptional catalytic stability after 10 000 cycles of a simulated start-up/shut-down stress test. The superior catalyst stability was explained with a lower Pt dissolution rate compared to carbon supported Pt electrocatalyst and the SMSI between Pt nanoparticles and Ta_{0.3}Ti_{0.7}O₂. Another class of stable carbon-free supports was found to be RuO₂/TiO₂ and RuO₂/SiO₂.^[14] These materials offer a conductivity and surface area comparable to mesoporous carbon, a promising electrochemical stability against aggressive accelerated test protocols besides improved membrane electrode assembly (MEA) performance. The incorporation of Pt nanoparticles with a well-defined size into the electrodes to decrease Ohmic and transport losses has to be improved to make it a viable alternative in automotive application. Furthermore, Dou et al. reported on tin oxide as another candidate for carbon-free support in PEFCs.^[15] The material retained 27% of its initial ECSA while the Pt/C reference catalyst shows almost no more surface area after 2000 cycles.^[15] In another approach, Tsukatsune et al. found that their Pt/SnO₂ and Pt/Nb-SnO₂ electrocatalysts suffer from low specific surface area accompanied with low specific activity.^[16] Cognard et al. investigated antimony-doped tin oxide supported Pt electrocatalyst as cathode material for PEFC.^[17] The harsh accelerated stress test (AST) conditions of potential jumps between 1.0 and 1.5 V lead to depletion of Sb atoms from the support surface and a decreased conductivity and hence to a loss in catalytic activity.

Indium tin oxide (ITO) offers several advantages in regard to the conditions that are present in the environment of fuel cell catalysts at the cathode site such as low pH, high temperatures, and high potentials. Additionally, ITO has the advantage of low electrical resistance. Pt/ITO catalyst systems have been tested as alternative material to conventional Pt nanoparticles dispersed on high surface area carbon. Liu et al. showed that a Pt/ITO ORR electrocatalyst offered activity as well as enhanced stability during an AST.^[18,19] These Pt nanoparticles were deposited on the ITO via a galvanic displacement of a Cu monolayer from a K₂PtCl₄ precursor. While the authors did not provide evidence for a complete displacement or removal of contaminating Cu residues, their data suggested that the enhanced ORR activity is caused by synergistic effects between surface Sn and Pt.^[19] A recent XPS study by Wang et al. of Pt/ITO as electrocatalyst for

PEFC MEAs revealed strong changes in the indium oxide component after operating conditions.^[20] These changes resulted in poor conductivity of the support followed by large activity losses. However, only little work has been done to understand how the entire catalyst/support couple and its components behave directly under AST-conditions with specific emphasis on Pt particle growth and agglomeration as well as support degradation. Deeper understanding of the catalyst during simulated fuel cell operating conditions will be crucial to develop a stable and active material.

In this study, we report new molecular insight in the degradation mechanisms of Pt/ITO electrocatalysts for oxygen reduction at fuel cell cathodes. What sets this study apart from previous ones is the use of a number of different in situ electrochemical X-ray and scanning flow cell-inductively coupled plasma (ICP) techniques to track the change in the molecular structure and composition of the catalysts during ORR catalysis. In situ high energy X-ray diffraction (HE-XRD) and anomalous small angle X-ray scattering (ASAXS) were applied to follow the structure and morphology of the Pt and ITO particles. In addition, scanning flow cell tests coupled to inductively coupled plasma mass spectroscopy (SFC ICP-MS), XPS, high angle annular dark field scanning transmission electron microscopy (HAADF-STEM) combined with energy-dispersive X-ray (EDX) spectroscopy yielded a deeper understanding of the evolution of morphology and surface composition after the ASTs. Together, our experimental study unravels critical parameters determining structural, morphological, compositional, and, thus, electrochemical stability of Pt on ITO.

2. Results

2.1. Physicochemical Characterization

Platinum nanoparticles supported on indium tin oxide have been synthesized using a solvothermal route using oleylamine and oleic acid as surfactants and dibenzylether as the solvent. The support material was introduced in the reaction mixture from the beginning to enable Pt nanoparticle growth directly on the support. Slow heating rates of 1 °C min⁻¹ were applied to obtain monodisperse Pt nanoparticles.

Figure 1 shows the XRD pattern of Pt on ITO as well as the pure ITO. All reflexes in the ITO pattern can be clearly assigned to an In₂O₃ phase (PDF#00-006-0416). No additional Sn oxide phase was present indicating complete incorporation of Sn into the In₂O₃ lattice thus, forming In_{2-x}Sn_xO₃ crystallites. The Pt/ITO pattern shows broad Pt reflections for pure face-centered cubic (fcc) Pt.

To analyze Pt particle size and Pt particle distribution on the support, transmission electron microscopy (TEM) was applied. **Figure 2a,b** shows quite homogeneously distributed Pt nanoparticles on the ITO support with an average size of 5.3 ± 0.7 nm (**Figure 2c**). Furthermore, the support consists of mostly well faceted nanocrystals with a size >10 nm. These crystals are randomly oriented and clearly distinguishable from the small Pt nanoparticles. The composition of the Pt/ITO as determined by inductively coupled plasma optical emission spectroscopy (ICP-OES) revealed a weight loading of 22.0 wt% Pt on ITO for the

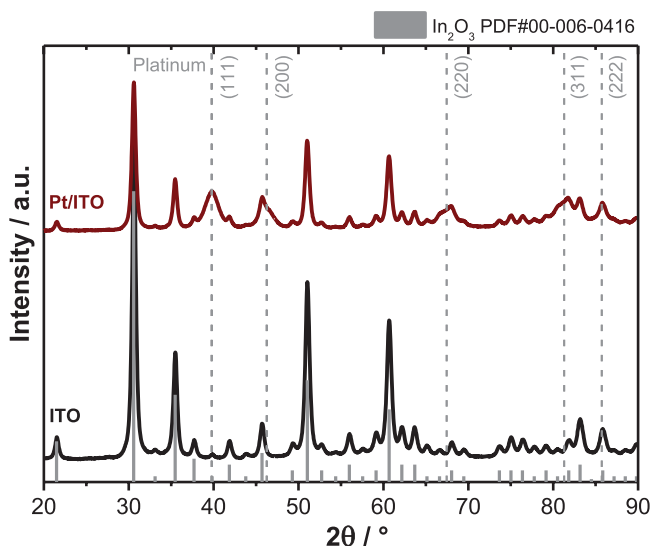


Figure 1. X-ray diffraction patterns of the bare ITO support material (black, bottom) and Pt/ITO catalyst (dark red, top) obtained using Cu $K\alpha$ radiation. Solid lines denote pure In_2O_3 reference pattern (PDF#00-006-0416). Vertical dashed lines denote reference powder diffraction patterns of fcc Pt (PDF#00-004-0802).

initial state (Figure 2a,b). This sample was used for low potential-AST (LP-AST) experiments. For all high potential (HP)-AST experiments the sample had a weight loading of 29.9 wt% Pt on ITO. Figure S1 (Supporting Information) shows TEM images and the corresponding histogram of the Pt particle size in the initial state. It can be clearly seen that Pt particle size and distribution as well as the shape and size of the support crystallites was almost identical compared to the sample with lower loading that was used for LP-AST.

2.2. Electrochemical Characterization

Figure 3a depicts the cyclic voltammograms (CVs) of the Pt/ITO catalyst in the initial state and after 5k CV in the lower potential region from 0.6–0.95 V versus reversible hydrogen electrode (RHE) (denoted as LP-AST). The ASTs were preceded and followed by CVs in the activation regime (0.05–1.00 V). It can be clearly seen that the CVs changed after the AST as the current in the Pt-O/OH region (0.6–0.8 V) drastically decreased. This suggests a lower number of oxidizable Pt sites on the nanoparticles after LP-AST. By contrast, the charge transferred in the H_{upd} region (0.05–0.4 V) decreased by only 8% as shown in **Figure 4** representing a minor loss in the hydrogen-based ECSA (H_{upd} -ECSA). The corresponding linear sweep voltammograms (LSV) in **Figure 3b** revealed a loss of the platinum mass-based activity (j_m) by 54% after LP-AST as evaluated at 0.9 V. To quantify the number of oxidizable Pt sites and to investigate their relation to the loss in mass activity, CO stripping experiments were performed at selected stages of the electrochemical stability test (Figure S3a, Supporting Information). **Figure 4** shows a comparison of ECSAs determined in the H_{upd} and CO oxidation region of the CO stripping experiment. Note that the absolute values of CO-ECSAs as presented in **Figure 4** are larger

compared to the H_{upd} based values due to a stronger adsorption of CO on Pt as it is well known from literature for Pt-based systems.^[21,22] However, it can be seen that the CO-ECSA decreased in the course of the LP-AST (–29%) measurement, whereas the H_{upd} -ECSA was rather stable (–8%). This also becomes clear as the ratio (CO/ H_{upd}) of both ECSAs decreased as seen by Table S2 (Supporting Information).

After the stability test in the higher potential range from 1.0–1.5 V (denoted as HP-AST) the cyclic voltammogram exhibited higher currents in the H_{upd} region compared to the initial state representing an increase of the H_{upd} -ECSA by 35% (Figure 3c). In contrast to the LP-AST, mass-based activity of Pt/ITO decreased by only 15% (Figure 3d) and the CO-ECSA by only 5% during the HP-AST (Figure 4). Thus, the catalytic activity of the Pt/ITO is significantly more stable in the HP-AST than in the LP-AST. However, in both cases the catalytic activity followed rather the CO-ECSA than the H_{upd} -ECSA.

To compare the Pt/ITO electrocatalyst to a commercial carbon supported material, a 20 wt% Pt/C reference catalyst was applied to the same ASTs. **Figure S2a,b** (Supporting Information) shows CVs and LSVs before and after the LP-AST. Pt/C exhibited higher stability in the lower potential regime than Pt/ITO with a loss in mass activity of only 14% (see also Table S1, Supporting Information). In contrast to that, the carbon supported catalyst showed a decrease of 38% in ORR mass activity after the HP-AST and an increase in H_{upd} -ECSA of 9% (Figure S2c,d, Supporting Information) suggesting a lower electrochemical stability than Pt/ITO in this potential regime.

To explain the changes in electrochemical surface area and catalytic activity toward the ORR, the evolution of the Pt particle size on ITO after the ASTs was analyzed by TEM (Figure 2d–i). The size of the Pt nanoparticles increased only slightly by around 1 nm from 5.3 ± 0.7 to 6.4 ± 0.9 nm after LP-AST (Figure 2d–e) which could explain the small decrease observed in H_{upd} -ECSA. Additionally, the edges of ITO nanocrystals appeared rather rounded compared to the faceted ITO crystallites of the initial state and the Pt particles seem to be more agglomerated.

After HP-AST (Figure 2g–i), the Pt nanoparticles did not grow as they exhibited an average diameter of 5.2 ± 0.6 nm. Therefore, the observed increase in H_{upd} -ECSA cannot be explained by the stable particle size distribution. In contrast to LP-AST, the nanocrystals of the ITO support did not only change in shape after HP-AST but also did not appear to be well separated anymore indicating coalescence to larger particles.

2.3. XPS and STEM/EDX Results

To get deeper insight into the changes of the Pt surface, XPS was performed on the Pt/ITO before and after the LP-AST and **Figure S4** (Supporting Information) shows the Pt 4f as well as the In and Sn 3d spectra of Pt/ITO. From the Pt 4f depth profile it can be seen that Pt in both samples is mostly metallic with a binding energy of around 71.1 eV (Figure S4a,b, Supporting Information). The initial state exhibited also a small fraction of PtO_x species (contribution at around 72 eV) which was significantly weaker at deeper probing depth of the photoelectrons and absent after the LP-AST. This finding is in agreement with the

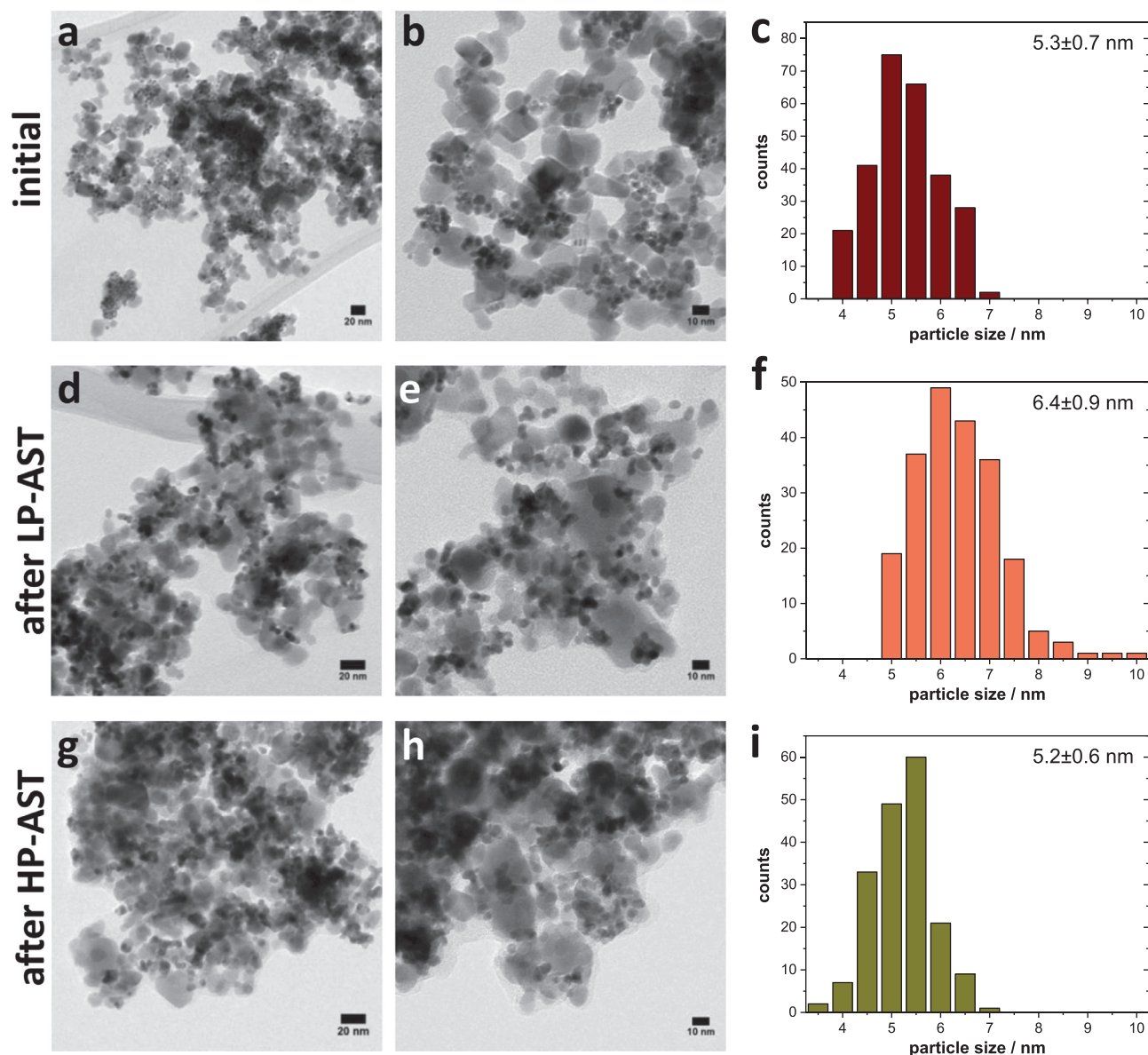


Figure 2. a,b) TEM images of the as prepared Pt nanoparticles on the ITO support, after electrochemical cycling for 5k times in d,e) lower potential region and in g,h) the higher potential region, as well as the corresponding histograms showing c,f,i) the particle size distribution. Histograms were obtained by measuring the diameter of at least 200 particles with errors obtained from standard deviation of mean particle diameter.

high resolution TEM (HR-TEM) micrographs in Figure S5c (Supporting Information) where a sub-nanometer amorphous shell around the metallic Pt nanoparticles is visible in the as-prepared state. This shell can be explained with a thin layer of Pt oxide around the nanoparticles that disappeared upon electrochemical cycling. The ITO was assessed by In and Sn 3d core levels (see Figure S4c,d, Supporting Information) and no difference was identified between the two analyzed states.

Table 1 shows the quantitative results from the XP spectra as obtained at two different positions of the sample. On the one hand the Pt/(In + Sn) ratio increased slightly indicating support leaching and furthermore, the In/Sn ratio changed toward lower Sn concentration. To analyze the Pt surface and the elemental distribution in more detail,

HAADF-STEM images and EDX maps were acquired. In Figure 5a,b the STEM-EDX mappings of a Pt nanoparticle deposited on ITO particles are shown before and after the LP-AST. Pt can be clearly distinguished from the support and no clear difference between the two states in terms of Pt particle size and elemental distribution is observed. In addition, In and Sn were homogeneously distributed in the ITO support and did not change drastically after potential cycling.

2.4. In Situ HE X-Ray Investigation

We performed in situ high energy XRD and SAXS to track and analyze the structural and morphological evolution of Pt

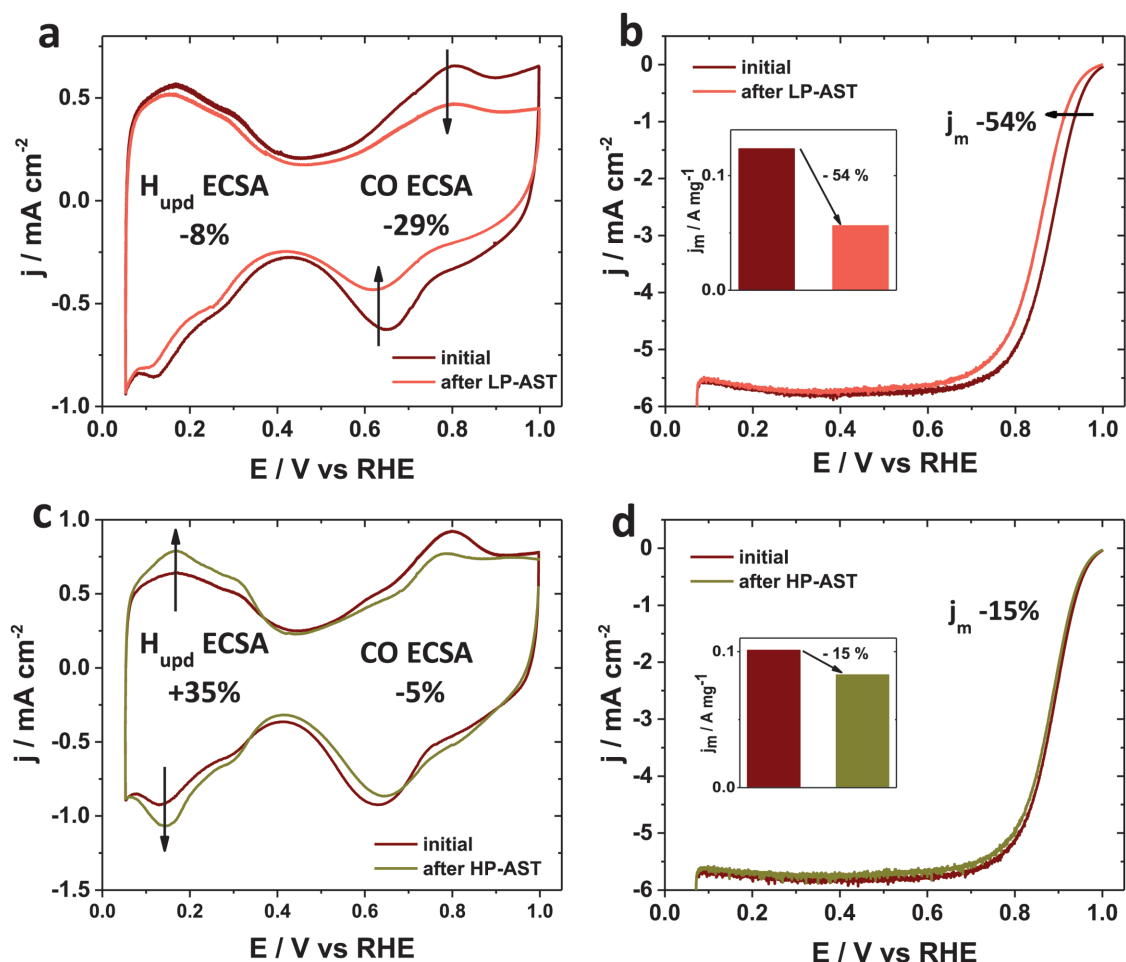


Figure 3. Cyclic voltammograms of Pt/ITO catalyst before and after potential cycling in a) lower and c) higher potential region. CVs were recorded in nitrogen saturated electrolyte from 0.05–1 V with a scan rate of 100 mV s⁻¹. b,d) LSVs of the particular states with the bar plots in the inlets representing the mass activity (j_m) evaluated at 0.9 V. LSVs were recorded in oxygen-saturated electrolyte from 0.05–1 V with a scan rate of 5 mV s⁻¹ and 1600 rpm. All electrode potentials have been corrected for iR drop.

particles as well as of In_{2-x}Sn_xO₃ crystallites during the AST and, thus, to gain deeper understanding about their degradation pathways. Figure S6a (Supporting Information) shows the evolution of X-ray diffraction patterns during the LP-AST including the initial state. It can be clearly seen that the Pt reflexes did not decrease in intensity whereas the intensity of the In_{2-x}Sn_xO₃ reflexes decreased drastically and thus, Pt/In_{2-x}Sn_xO₃ ratio increased. The results of Rietveld refinement (Figure 6a,b) show that the crystalline fraction of In_{2-x}Sn_xO₃ decreased from 79% to 61% during the LP-AST. The scale factor of the two crystalline phases (Figure S12a, Supporting Information) confirms the constant absolute amount of Pt and the loss of In_{2-x}Sn_xO₃ during LP-AST. Simultaneously, the Pt coherence length grew only slightly from the initial value of 4.33 ± 0.27 nm to 4.59 ± 0.27 nm, whereas the In_{2-x}Sn_xO₃ coherence length strongly increased from 13.89 ± 0.29 nm to 16.19 ± 0.46 nm. To gain a deeper insight in the evolution of the Pt nanoparticles, Pt-specific scattering curves were obtained from SAXS measurements around the Pt K-edge. Figure S7a (Supporting Information) shows the background-corrected scattering curves

with a clear feature visible above 0.1 Å⁻¹ resulting from Pt nanoparticles. By fitting these scattering curves and assuming a Gaussian distribution of spheres the particle size distribution (PSD) can be obtained (Figure S7b, Supporting Information). We identified a bimodal PSD with a high fraction (≈99%) of Pt particles with a size of around 4.5 nm and a small fraction (≈1%) of larger particles with a diameter of 9 nm. This finding shows that only a very slight fraction of the Pt particles was agglomerated.

The size of Pt nanoparticles stayed almost constant during the LP-AST but the agglomerated Pt particles shrink by ≈1 nm (Figure 6c). Additionally, we noticed a slight decrease in size of the Pt particles between the as-prepared state and the start of the stability test. Furthermore, we identified that the polydispersity σ of the Pt nanoparticles decreased slightly from 0.40 to 0.37. Thus, the results achieved by SAXS support the findings from Rietveld analysis and show the excellent morphological and structural stability of the Pt nanoparticles, which contrasts the evolution of the ITO support. Furthermore, we state that no significant loss in the absolute intensity of the Pt

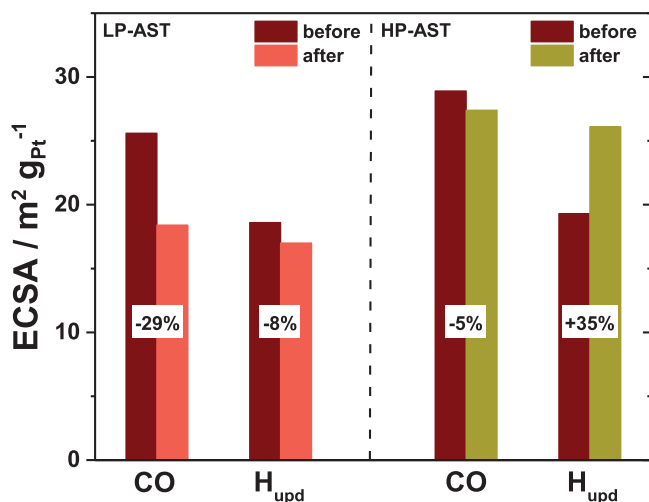


Figure 4. Comparison of ECSAs based on the integration in the H_{upd} and the CO oxidation potential range. CO-ECSAs were determined by integrating the CO oxidation peak area from the first cycle of the CO stripping experiment after subtraction of the second cycle representing the bare CO-free Pt surface. H_{upd} -ECSA was determined by subtracting the first from the second cycle of the CO stripping experiment.

scattering/reflections was obtained although the ITO support dissolved or became amorphous indicating a negligible loss of Pt nanoparticles.

Figure S6b (Supporting Information) shows the evolution of diffraction patterns during HP-AST and the intensities of the ITO reflexes decreased less strongly than during LP-AST. The evolution of fraction of the crystalline phases as determined by Rietveld refinement is shown in Figure 7a. It can be seen that the fraction of $\text{In}_{2-x}\text{Sn}_x\text{O}_3$ decreased by around 5% from 67% to 62%, whereas the Pt fraction simultaneously increased by the same extent. From the initial dry state to the state directly before the stability test an initial drop of the $\text{In}_{2-x}\text{Sn}_x\text{O}_3$ fraction of 3% was observed which can be explained with a partial dissolution (or amorphization) of the $\text{In}_{2-x}\text{Sn}_x\text{O}_3$ during the CVs in the activation regime. During the first 500 CVs of the HP-AST the $\text{In}_{2-x}\text{Sn}_x\text{O}_3$ fraction increased again. The scale factor of the two crystalline phases (Figure S12b, Supporting Information) confirms the loss of absolute amount of Pt and of $\text{In}_{2-x}\text{Sn}_x\text{O}_3$ during HP-AST. Throughout the whole HP-AST, the coherence lengths of both Pt and $\text{In}_{2-x}\text{Sn}_x\text{O}_3$ remained constant with a size of 4.25 ± 0.19 nm and 12.94 ± 0.44 nm, respectively (Figure 7b). Complementary to these in situ HE-XRD measurements, the results from ASAXS experiments show the stability of the Pt nanoparticles during the HP-AST as the mean particle

Table 1. Near-surface composition of Pt/ITO before and after LP-AST in the lower potential regime as obtained from XPS measurements. The molar ratios Pt, In, and Sn were determined from the peak areas of the Pt 4f as well as In and Sn 3d spectra recorded with a kinetic energy of the photoelectrons of 550 eV. The number in brackets denotes the composition at a second beam position of each sample.

	Pt/(In + Sn)	Sn/In
Initial	0.2 (0.21)	0.17 (0.17)
After LP-AST	0.25 (0.27)	0.14 (0.13)

size remained constant (Figure 7c) and the polydispersity σ increased slightly from 0.41 to 0.43 (Figure S8c, Supporting Information).

Generally, we state that perfect agreement between particle, crystallite size, and structural coherence length determination by TEM, (A)SAXS, and HE-XRD demands very high degree of homogeneity in shape, size, and crystallinity, which was not given in this study.^[23]

2.5. In Situ SFC ICP-MS

To differentiate between amorphization and dissolution/detachment of the ITO support and to track the dissolution of Pt, In, and Sn, experiments with an in situ SFC coupled to an ICP-MS were performed. The LP- and HP-ASTs were applied to the Pt/ITO and to the Pt/C reference catalyst.

Figure 8 shows the results from in situ SCF ICP-MS experiments for the two different potential regimes and it can be seen that a large dissolution peak arises for all three metals when the first contact between the electrode and the acidic electrolyte under open circuit potential (OCP) conditions was established (denoted as cell contact). During potential cycling in the activation regime Pt dissolution was observed in case of the ITO and C support. The Pt dissolution was up to $0.5 \mu\text{g}_{\text{det}} \text{L}^{-1} \mu\text{g}_{\text{WE}}^{-1}$ but limited to the first potential cycles (see Figure 8a) and no major difference between Pt/ITO and Pt/C was observed. No further Pt dissolution was observed during potential cycling in the activation and the LP regime.

During potential cycling in the activation and in the LP regime a low but constant dissolution of In and Sn was observed (0.05 and $0.1 \mu\text{g}_{\text{det}} \text{L}^{-1}$, respectively). Thus, the ITO dissolved continuously over the whole course of the applied electrochemical protocol without any specific potential dependence.

In case of the HP regime (Figure 8b) a relatively broad Pt dissolution peak can be observed for both carbon and oxide supports, but again, Pt dissolution was significantly more pronounced for Pt/C than for Pt/ITO. We determined the amount of Pt dissolution during the first cycles in the HP regime to be $1 \times 10^{-3} \mu\text{g}_{\text{det}} \mu\text{g}_{\text{WE}}^{-1}$ for Pt/C and $3 \times 10^{-4} \mu\text{g}_{\text{det}} \mu\text{g}_{\text{WE}}^{-1}$ for Pt/ITO (see also Figure S11, Supporting Information). Note that Pt dissolution becomes more pronounced during the activation potential cycles after the potential cycling in the HP regime compared to that in the LP regime. A likely explanation is the reductive dissolution of the electrochemically formed PtO_x species.^[2,24] Pt-specific dissolution behavior with a small oxidative dissolution peak and a big and sharp peak in the reductive scan of the AST were superimposed by a broad and decreasing dissolution signal due to the relatively high scan rate of 500 mV s^{-1} in the HP-AST.

In addition to the dissolution peaks of In and Sn upon first cell contact, a small Sn dissolution peak was observed at the beginning of the activation regime which remained comparable in intensity to Sn dissolution during the LP-AST. Slight In and a more pronounced Sn dissolution was also detected during the first cycles in the HP regime and, thus, the observed Pt loss was likely caused by Pt nanoparticle detachment due to support dissolution. Data evidence that Sn is more prone to dissolve during the HP-AST. Generally, we state that only 0.04% (0.10%)

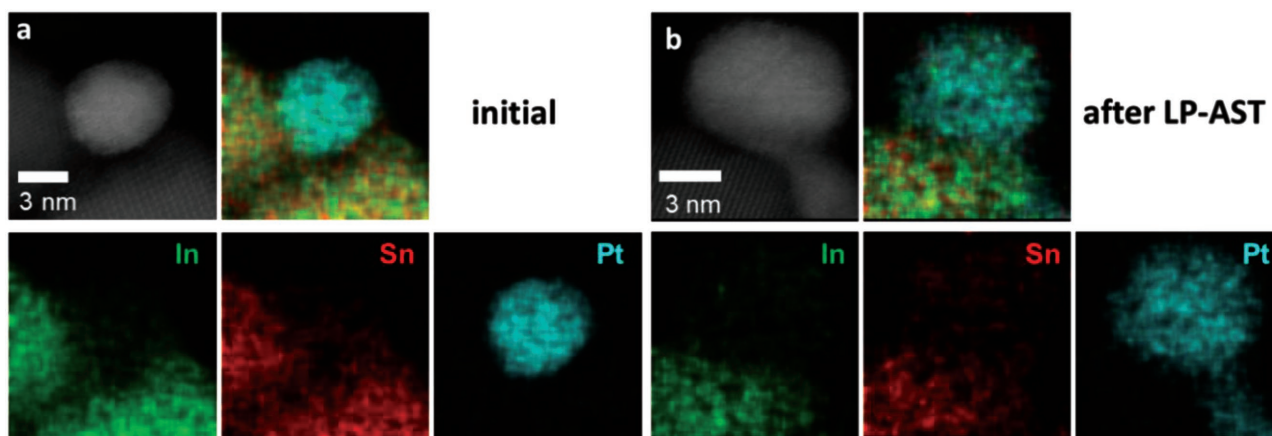


Figure 5. HAADF-STEM images and EDX mapping of a) Pt/ITO initial and b) after LP-AST. Platinum is depicted in light blue, indium in green, and tin in red.

of Pt and 1.89% (2.47%) of the ITO support was dissolved over the whole course of the applied though shorter electrochemical protocol for the LP (HP) regime. For comparison, in case of the Pt/C reference 0.09% (0.29%) of the total Pt mass was dissolved (see also Table S3, Supporting Information).

3. Discussion

Associated with the need of developing new and stable electrocatalysts for PEFCs, an in situ stability study of ITO-supported Pt nanoparticles has been conducted. We were able to successfully deposit Pt nanoparticles with a uniform size on the highly crystalline support. The catalyst was tested for electrochemical stability under simulated fuel cell conditions by applying two different ASTs representing conventional operating conditions (0.6–0.95 V) and start-up/shut-down (1.0–1.5 V). By employing a wide range of in situ (X-ray) techniques as well as advanced spectroscopy and electron microscopy we aimed to determine fundamental descriptors for electrochemical catalyst and support stability as well as the most prominent degradation pathway.

Electrochemical Versus Structural Stability. The investigation of electrocatalytic stability in acidic media applying two

different protocols has revealed that Pt/ITO shows higher electrochemical stability in the HP-AST than in the LP-AST. In particular, ORR activity and CO-ECSA decreased strongly during the LP-AST, while H_{upd} -ECSA stays rather stable, suggesting that the CO-ECSA is a better descriptor for the ORR active site density. These findings show that the Pt surface after LP-AST remains accessible for H adsorbates represented by a stable H_{upd} -ECSA but not for O/OH adsorbates which are essential for the oxygen reduction reaction. TEM analysis shows almost no growth of Pt nanoparticles and a slightly higher degree of Pt agglomeration. This slightly higher degree of agglomeration of the Pt particles can explain the small decrease of the accessible surface area as measured via H_{upd} but the CO-ECSA decreased to a higher extent. In situ X-ray investigations again proved that Pt particle and crystallite size was stable over the LP-AST and in situ SFC ICP-MS showed negligible Pt dissolution. The morphological and structural stability of the Pt nanoparticles contrasts the strong loss in catalytic activity.

Thus, the major changes in ITO indicate a strong influence of the morphological stability of ITO on the catalytic activity of Pt. In situ X-ray investigations revealed that the fraction of crystalline ITO strongly decreased and the crystallite size increased. Hence, the ITO is partially dissolved/detached or loses crystallinity during LP-AST. From in situ SFC ICP-MS

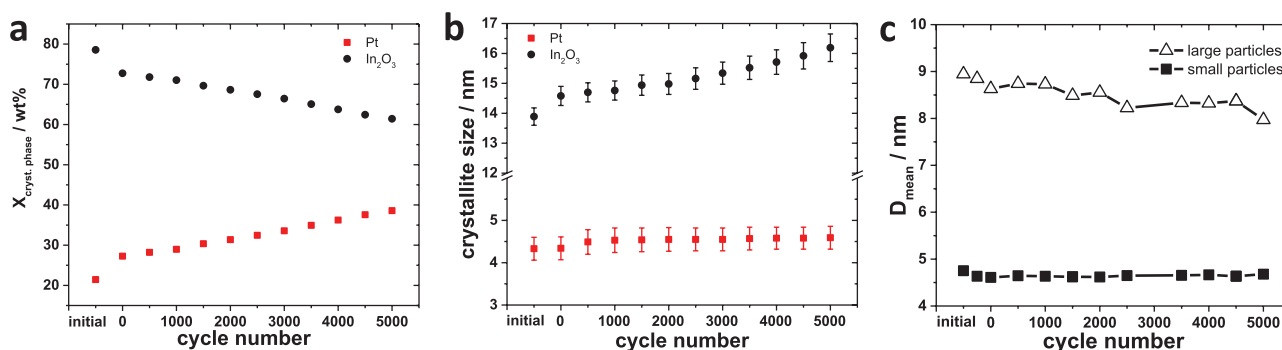


Figure 6. Results from in situ HE-XRD and ASAXS measurements for LP-AST. Weight fractions of a) crystalline phases and b) their coherence lengths as determined by Rietveld refinement. c) Mean Pt particle diameter was determined from fitting of ASAXS curves.

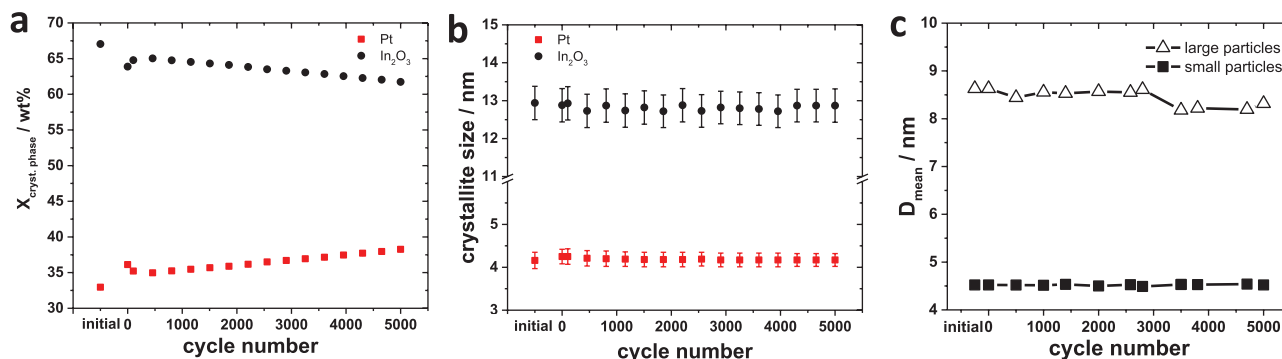


Figure 7. Results from in situ HE-XRD and ASAXS measurements for HP-AST. Weight fractions of a) crystalline phases and b) their coherence lengths as determined by Rietveld refinement. c) Mean Pt particle diameter was determined from fitting of ASAXS curves.

measurements a small but continuous dissolution of In and Sn was observed, but the observed loss from HE-XRD in ITO weight fraction is much higher suggesting partial amorphization of ITO. Dissolved In/Sn ions are prone to be (electro)chemically and isostructurally redeposited on the ITO crystallites which can explain the determined growth via Ostwald ripening.^[25] Alternatively, the loss of smaller crystallites would lead to a larger mean crystallite size.

We have to note that the loss of crystalline ITO is not directly linked to a loss of Pt nanoparticles. Rietveld refinement shows that the absolute amount of Pt remained stable during the LP-AST, whereas the absolute amount of crystalline ITO strongly decreased (as measured by the scale factor extracted from fits of the HE-XRD pattern, see Figure S12a of the Supporting Information). These findings suggest that ITO gets preferentially dissolved where locally no Pt is present and that the Pt nanoparticles might be stabilizers of ITO. By acting as electron scavenger the Pt inhibits the electrochemical reduction

of the surface In/Sn ions and thus, reduces their dissolution into the electrolyte. This function is similar to the role of an appropriate cocatalyst on photoanodes acting as hole scavengers leading to enhanced photoelectrocatalytic stability.^[26] Thus, we can conclude that while Pt is almost unaffected by the conditions present during LP-AST, the strong changes of the ITO influence the stability of the electrocatalytic activity of the Pt nanoparticles.

The AST in the HP regime from 1.0–1.5 V revealed a significantly better stability of the catalytic activity. TEM analysis and in situ X-ray results showed that ITO nanocrystals and Pt nanoparticles did not grow and the composition remained stable compared to the LP-AST. This agrees with a rather stable CO-ECSA and hence with a stable mass-based activity, which again shows the dependency of these two descriptors. By contrast, the Pt surface area became larger as it exhibited a higher H_{upd} -ECSA. This can be explained by an electrochemical roughening of the Pt surface as elevated Pt dissolution was observed

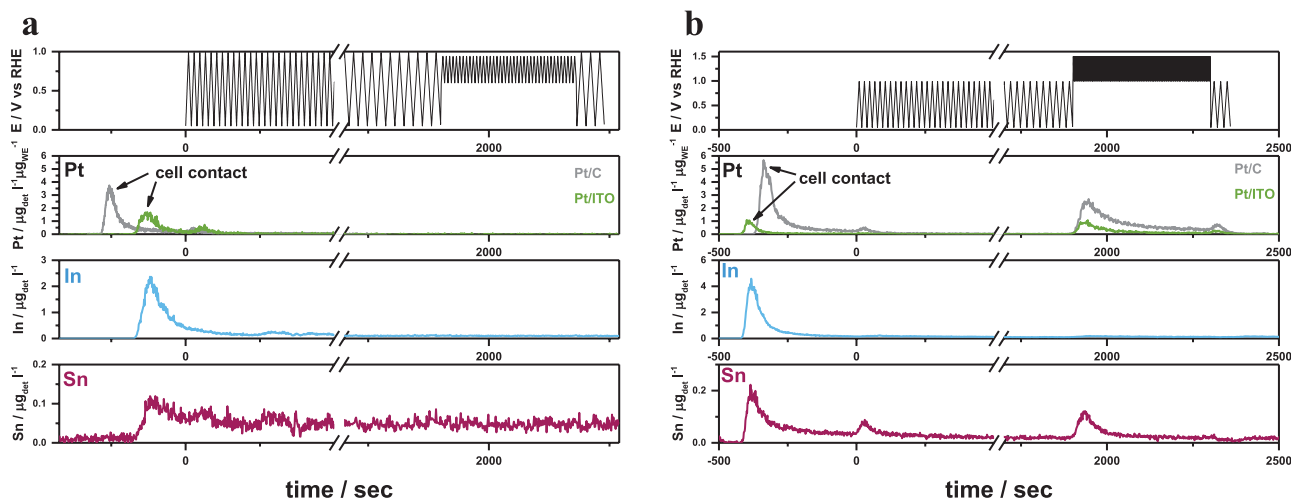


Figure 8. In situ scanning flow cell ICP-MS measurements. Depicted are the Sn, In, and Pt dissolution rates and the applied electrochemical protocols from the bottom to the top for a) LP-AST and b) HP-AST. The respective dissolution rates in detected (det) metal in μg per volume electrolyte ($\mu\text{g}_{\text{det}} \text{l}^{-1}$) are plotted against the time. A Pt/C reference sample was measured and therefore, the Pt dissolution rate was also normalized to the Pt mass loading on the working electrode (WE) ($\mu\text{g}_{\text{det}} \text{l}^{-1} \mu\text{g}_{\text{WE}}^{-1}$). The electrochemical protocol was conducted as follows: Beginning with 100 CVs (activation regime) from 0.05–1 V, followed by potential cycling in the LP regime (0.6–0.95 V, 40 CVs, 100 mV s^{-1}) or in the HP regime (1.0–1.5 V, 200 CVs, 500 mV s^{-1}) and followed by another 3 cycles from 0.05–1 V, all CVs were recorded with a scan rate of 100 mV s^{-1} . The first contacts between catalyst and electrolyte (cell contact) are denoted with arrows. Breaks at the time axis of (a) and (b) have been implemented between 500 and 1700 s. Graphs with complete time axis can be found in Figures S9 and S10 of the Supporting Information.

from in situ SCF ICP-MS during the HP-AST. Furthermore, the dissolved Pt ions could be redeposited on the cathode as sub-nanometer clusters or single atom sites which we did not detect by electron microscopy and HE-XRD. But these domains would contribute to the increase in the H_{upd} -ECSA and would lower the dissolution rate with respect to the loss of crystalline Pt nanoparticles. The Pt dissolution during HP-AST was accompanied by small In and more pronounced Sn dissolution affecting the shape of the ITO crystallites as observed in TEM images. However, these changes influenced the structure and morphology of the ITO less strongly than during the LP-AST and without a tremendous impact on the catalytic performance. Additionally, the loss of crystalline $\text{In}_{2-x}\text{Sn}_x\text{O}_3$ from in situ HE-XRD could rather be assigned to support leaching than to amorphization as concluded for LP-AST.

The comparison of the electrochemical results revealed a higher stability for the Pt/C reference in the LP-AST when compared to the Pt/ITO catalyst. Dissolution of Pt in Pt/C during the LP-AST was very low and comparable to that of Pt/ITO, indicating similar morphological Pt stability in Pt/C and Pt/ITO. After HP-AST the reference material revealed a lower stability with a relatively big loss in catalytic activity. From in situ ICP-MS it can be seen that during cycling in the range of 1.0–1.5 V Pt dissolution was much more pronounced in Pt/C than in Pt/ITO. This can be explained with a stronger electronic interaction between the metal particles and the oxide support impeding nanoparticle detachment or dissolution but could also be caused by the differences in particle size and, thus, electrochemical surface area. In that respect, initial Pt dissolution peaks at cell contact due to PtO_x reduction at OCP conditions were again smaller for ITO supported Pt. ITO might decrease PtO_x formation resulting in lower peak intensity compared to the Pt/C reference.

Catalyst/Support Degradation Pathways: From the above described electrochemical and structural behavior of Pt/ITO under operating conditions we conclude that the support stability has a tremendous impact on the stability of the catalytically active sites. We are able to exclude well-known catalyst degradation phenomena caused by Pt particle growth, agglomeration, and dissolution/detachment and propose a pathway based on strong influence of support degradation on the availability of Pt active sites. In detail, we found an overall excellent structural and morphological stability of Pt but we determined altering of the ITO support as a likely actuator for Pt (surface) poisoning and resulting performance loss in the ASTs, especially in the LP-AST.

For the LP-AST, XPS data indicate support loss in the form of Sn leaching and continuous but small support dissolution was also found by in situ ICP-MS. The dissolved metal ions could be electrochemically redeposited not only preferentially on the ITO surface but also on the Pt surface during the relative reductive conditions of cycling between 0.6 and 0.95 V. The increasing Pt/(In + Sn) ratio from XPS after LP-AST is dominated by the preferential dissolution (or detachment) of the support but does not exclude Pt surface modification.

Consequently, we aim to uncover the origin for this poisoning effect in the form of proposed degradation pathways. Possible mechanisms for Pt surface poisoning could be (a) support metal incorporation into Pt nanoparticles leading to alloy

formation, (b) formation of an amorphous metal (oxyhydr)oxide layer, or (c) redeposition of In and/or Sn ions on the Pt surface.

Metal diffusion into Pt leading to alloy formation preferentially due to Sn alloying into the Pt lattice could also lower catalytic activity. In that respect, no other phase was observed during potential cycling in the HE-XRD. Nevertheless, the evolution of Pt lattice constant based on Rietveld refinement during the LP-AST was tracked, because Partial PtSn alloy formation should increase the lattice constant (PtSn₃, PDF#00-035-1360). Figure S13a (Supporting Information) shows the lattice constant as a function of the cycle number in the LP-AST. Here, it can be seen that the lattice constant decreases from beginning to end of cycling. Furthermore, the formation of a near-surface alloy leading to a PtSn shell is unlikely because this would lead to a decrease of the Pt coherence length. Thus, PtSn alloy formation is unlikely and can therefore be excluded for the major Pt poisoning contributors.

Another interpretation of the combination of electrochemical and in situ results can be the partial transformation of ITO to an amorphous $\text{In/SnO}_x(\text{OH})_y$. This (oxyhydr)oxide formation could then lead to a (partial) encapsulation in the form of a thin (mono)layer around Pt. This theory would go in line with relatively strong loss of crystalline $\text{In}_{2-x}\text{Sn}_x\text{O}_3$ fraction from HE-XRD and only little In and Sn dissolution from ICP-MS. Such a layer would be permeable for protons but not for larger molecules like CO or OH and could thus, explain the different trends in H_{upd} - and CO-ECSA. This phenomenon, also known as “decoration effect,” originates from SMSI and is well known in literature for different metals (Rh, Pt, Pd, Ni, Co) supported on metal oxides (TiO_2 , Fe_3O_4 , WO_x).^[27] In these studies, the encapsulation has been induced by thermal/chemical reduction of the oxide support as well as electrochemical reduction at low potentials in the case of Pt/ WO_x . In our case, the LP-AST in acidic electrolyte implies reductive reaction conditions for the oxide support. In photocatalysis this effect is intentionally induced to suppress ORR in hydrogen evolution catalysts by growing a proton- and hydrogen-permeable Cr_2O_3 shell around an Rh catalyst. This shell is impermeable for O_2 molecules inhibiting undesired ORR.^[28] We identified a marginal growth of Pt particles by less than 1 nm in TEM micrographs after LP-AST (Figure 2), while the coherence length/domain size (as obtained by HE-XRD) and particle size (as obtained by SAXS) remained constant. This finding would go in line with the formation of sub-nanometer (oxyhydr)oxide layer around Pt but can also be within the error of particle size estimation from TEM due to higher degree of agglomeration. However, we could not prove the formation of this layer by STEM images and EDX spectroscopy even though a sub-monolayer coverage or adsorption might be hard to detect. Also XP spectroscopy does not give the sensitivity to differentiate between the chemically unchanged isostructurally grown $\text{In}_{2-x}\text{Sn}_x\text{O}_3$ crystallites and sub-monolayer coverage of the support metal ions on the surface of the Pt nanoparticles. However, we expect the ad-atoms to differ chemically from the Sn/In ions in the $\text{In}_{2-x}\text{Sn}_x\text{O}_3$.

It is known from literature that In and/or Sn metal adsorbates present as sub-monolayer on Pt single crystal surfaces can strongly affect the CO oxidation behavior.^[29] Therein, adsorbed Sn on various Pt surfaces lead to a growth of the oxidation peak at 0.53 V. In case of the Pt (111) surface Sn coverage blocks the

more anodic CO oxidation peak at 0.65 V, whereas it does not affect the CO electrooxidation on Pt (100) and (110) surfaces. CO electrooxidation on the Pt/ITO catalyst also shows a preferential poisoning of the high potential oxidation peak after the LP-AST, and thus, our electrochemical data are in agreement with the surface poisoning of the Pt nanoparticles with metal (Sn) ions (Figure S3, Supporting Information). We note that the anodic shift of the CO oxidation potential might be caused by the In adsorbates in addition to Sn. In another approach, Pt supported on Nb- and Sb-doped SnO₂ was used as catalyst for single cell stability tests and it was found that Sn was dissolved at reducing potentials resulting in Pt poisoning by Sn redeposition.^[30] Nakada et al. studied SnO₂ supported Pt electrocatalyst and they found decreased Pt oxidation/reduction current due to stronger interactions of Sn with Pt after electrochemical cycling.^[31] Additionally, under potential deposited (UPD) Sn on Pt was found to change the Pt oxidation behavior when cycling in HClO₄.^[32]

In case of the HP-AST the dominant degradation mechanism is Pt dissolution from PtO_x species by reaching potentials as high as 1.5 V. Interestingly, ITO support dissolved as well in this potential regime leading to support modification, but did not affect the electrochemical performance drastically. We explain that with the slight but continuous dissolution of surface Pt atoms under oxidative conditions, which continuously pours away potentially adsorbed In/Sn atoms. This process prevents significant poisoning with In/Sn atoms and, thus, leads to a rather stable mass-based catalytic activity. Furthermore, cathodic potentials as low as 0.6 V as in LP-AST might be required to form metal (oxyhydr)oxides or Sn UPD layer on the Pt surface.

For the HP-AST regime we clearly established a superior structural stability of Pt nanoparticles on ITO versus C supports. Some earlier work put forward strong electronic interactions between metal particles and the oxide support impeding nanoparticle detachment.^[13,33] Recent DFT calculations showed that the electronic influence of oxide support is limited to a few atom layers of Pt.^[34] The Pt nanoparticles in this work are significantly larger and, thus, electronic interactions may remain masked from spectroscopic identification although they are indeed anchored more strongly to oxide supports.

Combining all these results, we propose that the activity loss during the LP-AST is caused by a kind of Pt surface modification due to In and, more likely, Sn accumulation. During HP-AST this degradation pathway is blocked because slight anodic dissolution of Pt keeps the active sites accessible.

4. Conclusion

We have explored the stability and degradation of Pt nanoparticles supported on ITO support during the electrocatalytic reduction of molecular oxygen as well as during two distinct degradation regimes corresponding to normal fuel cell operation and a start-up/shut-down operation, respectively. The Pt/ITO electrocatalyst consisted of monodisperse, well-distributed Pt particles with a size of around 5 nm and was investigated using a number of different *in situ* techniques (i) to gain fundamental insight in the degradation mechanisms, (ii) to

unravel fundamental descriptors of structural and morphological stability, and (iii) to determine stability limitations of this material system. Our combination of X-ray and electron microscopic techniques has advanced our understanding of the fundamental processes associated with the degradation behavior of Pt/ITO electrocatalysts.

Under catalytic ORR operation conditions (LP-AST) we have demonstrated that Pt nanoparticles remain morphologically stable and degradation pathways due to Pt instability can be excluded, whereas the ITO support suffers from cathodic corrosion coaffecting the catalytic stability and mechanical/chemical attachment of the Pt nanoparticles. ITO crystallites partially dissolve, become amorphous, and grow via an Ostwald ripening mechanism. Therefore, we have strong indications that the significantly declined catalytic ORR activity after LP-AST is attributed to partial In/Sn redeposition and concomitant surface decoration of active Pt particle. Such oxidic Pt surface adlayers change the Pt redox chemistry and lower the density of specific O-adsorption sites. An encapsulation of the Pt nanoparticles with an (oxyhydr)oxide layer could equally account for this behavior, yet was not fully supported by the available data. By contrast, during start-up/shut-down cycles (HP-AST), the catalyst/support couple showed excellent stability, thanks to the improved structural and morphological durability of the oxide support compared to the commercial Pt/C couple. We found evidence for slight continuous anodic Pt dissolution which aided in suppressing Pt surface poisoning and thus stabilizing the available active site density.

Overall, this study has unraveled the major degradation pathways of ITO-supported Pt nanoparticle fuel cell catalysts over wide cathode potential ranges; our findings advance our understanding of the fundamental aspects of support stability. They are also of practical value for the development of improved fuel cell devices, as they offer design criteria and performance limitations of oxide-based PEFC cathode catalysts.

5. Experimental Section

Synthesis of ITO: In(Cl)₃ (1.434 g, Strem Chemicals) was dissolved in deionized water (2.16 mL) and the solution was stirred for 10 min. Then SnCl₄ (79.2 μL, Acros Organics) was added to the solution under stirring for 10 min followed by addition of ethanol (9 mL, 200 proof). Afterward propylene epoxide (5.5 mL, Sigma-Aldrich) was added drop-by-drop to the alcoholic solution at room temperature under continuous stirring for 15 min. When the solution turns milky, stirring was continued for another 10 s and put into an ice bath afterward for 10 min. The resulting gel was aged for 10 h and then subjected to a series of solvent exchange in acetone (Fischer Scientific) for 10 times in 3 d. The acetone-loaded gels were then introduced into a supercritical dryer (SFT-100, Supercritical Fluid Technologies, Inc.), and the acetone was removed using supercritical CO₂ extraction (45 °C and 275.8 bar). The dry gel was further calcined at 820 °C for 150 min in air.

Synthesis of Pt Nanoparticles on ITO: Platinum nanoparticles were synthesized using a solvothermal synthesis route based on previous work.^[35] In detail, Pt(acac)₂ (0.6 mmol, Alfa-Aesar, Pt 48% min), 1,2-tetradecanediol (1.2 mmol, 90%, Sigma-Aldrich), oleylamine (300 μL, ≥98%, Aldrich), oleic acid (300 μL, 90%, Alfa Aesar), and 100 mg ITO were dispersed in dibenzylether (50 mL, 98%, Fluka). The mixture was stirred under nitrogen atmosphere to remove excess of oxygen. Then, the temperature was raised to 80 °C and held for 5 min to ensure complete dissolution of the Pt precursor and the reducing agent.

Afterward the temperature was raised with the ramping of $1\text{ }^{\circ}\text{C min}^{-1}$ to $165\text{ }^{\circ}\text{C}$ and kept for 1 h. The mixture was cooled down to room temperature and ethanol (80 mL, 100%, VWR Chemicals) was added, followed by sonication with an ultrasonic horn for 1 h and stirring overnight. The supernatant was removed by centrifugation (7800 rpm, 15 min) and washed with ethanol (40 mL) three times. The received catalyst was freeze dried overnight.

XRD: Lab-based X-ray diffraction patterns were measured on a Bruker D8 Advance diffractometer in Bragg Brentano geometry using Cu K_{α} radiation with a wavelength of 0.154 nm between 20° and 90° using a step size of 0.04° and 7 s time at each step.

ICP-OES: Compositional analysis was performed using an inductively coupled plasma analysis system (Varian 715-ES). The concentration of the standards was 1, 5, and 10 mg L^{-1} and the wavelengths for the Pt measurement were 203.646, 204.939, 212.863, 214.424, 217.468, 224.552 nm.

TEM: TEM micrographs were recorded on a FEI Tecnai G² 20 S-TWIN with a LaB₆ cathode operating with 200 kV acceleration voltage and a resolution limit of 0.24 nm . Samples were dispersed in ethanol with an ultrasonic horn, drop casted on a Cu grid, and dried in air at $60\text{ }^{\circ}\text{C}$ for 7 min.

HR-TEM was performed using a FEI Titan 80–300 TEM electron microscope with a C_s corrector for the objective lens (CEOS GmbH). The microscope was operated at 300 kV.^[36]

HAADF-STEM and EDX Spectroscopy: STEM was performed using a FEI Titan G² 80–200 (“ChemiSTEM”) electron microscope with a C_s-probe corrector (CEOS GmbH) and a HAADF detector.^[37] The microscope was operated at 200 kV. In order to achieve “Z-Contrast” conditions, a probe semi-angle of 25 mrad and an inner collection semi-angle of the detector of 88 mrad were used. Compositional maps were obtained with EDX using four large-solid-angle symmetrical Si drift detectors. For EDX elemental mapping, Pt L, Sn L, and In L peaks were used.

Electrochemical Characterization—Catalyst Ink Preparation: Catalyst powder (6 mg) was added to water (1.99 mL), ¹PrOH (500 μL , $\geq 99.95\%$, Sigma-Aldrich) and Nafion solution (10 μL , 5 wt%, Sigma-Aldrich) and sonicated using an ultrasonic horn for 30 min. 10 μL of the ink was drop casted on a 5 mm diameter glassy carbon (GC) electrode and dried in air at $60\text{ }^{\circ}\text{C}$ for 7 min. The GC electrodes were pretreated by polishing in two steps using Buehler alumina polishing solution with diameter 1.0 and $0.05\text{ }\mu\text{m}$. A geometric Pt loading of around $25\text{ }\mu\text{g}_{\text{Pt}}\text{ cm}^{-2}$ was obtained.

Electrochemical Characterization—Rotating Disc Electrode (RDE): A commercial three electrode cell was used for electrochemical characterization consisting of a Pt mesh (furled Pt $5 \times 5\text{ cm}^2$) as counter electrode and a mercury/mercury sulfate reference electrode (Hg/Hg₂SO₄, Ametek, potential -0.722 V vs RHE). 0.1 M HClO_4 (diluted with Mili-Q from 70% HClO₄, 99.999% trace metal bases, Sigma-Aldrich) was used as electrolyte for all electrochemical measurements. A SP-150 or SP-200 Potentiostat (BioLogic Instruments) was used to control the potential of the working electrode (WE) and a commercial AFMSRCE rotator (Pine Research) to control rotation. The degree of purity for the used gases was 99.998% for oxygen, 99.999% for nitrogen, 99.999% for hydrogen, and 99.997% for CO. All potentials are referred to the RHE.

Electrochemical Characterization—CV: CVs were recorded between 0.05 and 1 V with a scan rate of 100 mV s^{-1} for 100 cycles under nitrogen atmosphere.

Electrochemical Characterization—LSV: LSVs were recorded between 0.05 and 1 V with a scan rate of 5 mV s^{-1} and a rotation speed of 1600 rpm under oxygen atmosphere. Determination of the kinetic currents was done by applying the following Equation (1)

$$\frac{1}{j} = \frac{1}{j_k} + \frac{1}{j_d} \quad (1)$$

Here, j is the current at 0.9 V, whereas j_d was determined by averaging the diffusion limited current between 0.1 and 0.6 V and j_k is the calculated current density (mass and geometric based).

Electrochemical Characterization—CO Stripping: First, the electrolyte was saturated by bubbling with nitrogen for 15 min. Afterward the

working electrode was immersed into the electrolyte at 0.05 V and 400 rpm and the gas was switched to CO. CO was then bubbled through the electrolyte for 15 min to ensure complete coverage of the Pt surface with CO. Afterward nitrogen was bubbled for another 15 min to remove excess CO from the electrolyte. CO stripping was performed by cycling between 0.05 and 1 V for 5 cycles with a scan rate of 50 mV s^{-1} . ECSA determination based on the area of the CO oxidation peak and hydrogen under potential deposition (H_{upd}) was done by subtracting the first two consecutive cycles of the stripping protocol and integration of the charge between the two cycles.^[22] The measured Q_{CO} or Q_{H} values were normalized with respect to the theoretical values for a two electron transfer $Q_{\text{CO}}^{\text{theo}} = 420\text{ }\mu\text{C cm}^{-2}$ in case of CO as probe molecule and to the theoretical value for a one electron transfer $Q_{\text{H}}^{\text{theo}} = 210\text{ }\mu\text{C cm}^{-2}$ in case of desorption of hydrogen.

Electrochemical Characterization—Stability Test: Stability measurements in the LP regime were performed between 0.6 and 0.95 V for 5k cycles with a scan rate of 100 mV s^{-1} under nitrogen atmosphere and with the 22.0 wt% Pt/ITO sample. Stability measurements in the HP regime were performed between 1.0 and 1.5 V for 5k cycles with a scan rate of 500 mV s^{-1} under nitrogen atmosphere and with the 29.9 wt% Pt/ITO sample. Before and after these protocols three CVs between 0.05 and 1 V with a scan rate of 100 mV s^{-1} were performed. Parameters for both stability tests (potential range, scan rate, etc.) were adapted from the US Department of Energy (DoE) fuel cell targets from the year 2016.

A 20 wt% Pt/C catalyst (Pt on Vulcan Carbon, BASF) was used as reference material for RDE stability measurements.

All presented electrode potentials were iR-corrected by the high frequency resistance R_{HF} determined by potentiostatic electrochemical impedance spectroscopy at 0.5 V. All measurements were repeated at least three times in order to ensure reproducibility.

In Situ HE-XRD and ASAXS: In situ XRD and ASAXS measurements were performed at beamline ID 31 at the European Synchrotron Radiation Facility (ESRF) in Grenoble. Diffraction patterns were recorded using a monochromized X-ray beam (77 keV) focused to $200 \times 6\text{ }\mu\text{m}^2$ using a large area Pilatus3X CdTe 2M detector. A transmission cell with a three electrode setup was used for the in situ measurements.^[3]

For the working electrode a carbon paper sheet was covered 10 times with 10 μL of ink dispersion and consecutive drying in air at $60\text{ }^{\circ}\text{C}$ for 8 min. A Pt wire acted as counter electrode and a 3 M Ag/AgCl reference electrode (freshly calibrated against Pt/H₂ electrode) was used. Electrochemical protocols were applied using a SP-200 Potentiostat (BioLogic Instruments). Diffraction patterns were corrected by the background. The working distance was calibrated using a CeO₂ standard (NIST SRM 674b) and Ag Behenate for SAXS.

ASAXS curves were obtained by subtracting the background-corrected and transmittance-normalized scattering curves recorded at 77 and 77.8 keV. The energy of the beamline was aligned using the Pt K-edge absorption spectrum. Fitting of the ASAXS scattering curves was performed using the software package SASfit assuming Gaussian size distribution of spherical particles and a form factor representing a hard sphere was taken into account.

XPS: X-ray photoelectron spectroscopy measurements were performed at the ISSS beamline of BESSY II facility operated by Helmholtz Zentrum Berlin. The catalyst ink was drop casted onto a 5 mm diameter glassy carbon disc and dried for 7 min at $60\text{ }^{\circ}\text{C}$. The catalyst was treated by the electrochemical protocol described above including the stability test in the low potential regime. XPS measurements were conducted in ultrahigh vacuum (UHV) at room temperature. Pt 4f depth profiling was accessed by using kinetic energy of the photoelectrons of 210, 550, and 1200 eV.

In Situ SFC ICP-MS: Catalyst inks of Pt/C and Pt/ITO were prepared with a solution of 5% Nafion (25 μL , Sigma-Aldrich) and ultrapure water (4.975 mL, 18.2 M Ω , PureLab Plus System, Elga), with an appropriate amount of catalyst powder in order to obtain a final loading of $\approx 1.6\text{ }\mu\text{g}_{\text{Pt}}\text{ cm}^{-2}$. A glassy carbon sheet (SIGRADUR G, HTW) was polished with $1\text{ }\mu\text{m Al}_2\text{O}_3$ suspension and extensively rinsed with ultrapure water. The ink was sonicated and subsequently 0.3 μL drops

were pipetted onto the glassy carbon sheet. The formed spots on the glassy carbon sheet of $\approx 0.01 \text{ cm}^2$ were used as working electrodes.

Electrochemical and dissolution (Pt, In, and Sn) measurements were carried out using the previously described SFC ICP-MS (NexION 300X, Perkin Elmer) setup.^[38] The cell contact area was 0.035 cm^2 . A saturated Ag/AgCl and graphite rod were used as reference and counter electrodes, respectively. Potentials are reported against RHE, which was measured daily prior to experiments. Measurements were carried out in a flow of 0.1 M HClO_4 prepared from ultrapure water and Suprapur 70% perchloric acid (Merck), with continuous argon purging. The flow rate of the SFC ICP-MS was $\approx 170 \mu\text{L min}^{-1}$, while $10 \mu\text{g L}^{-1}$ ^{187}Re for Pt and $20 \mu\text{g L}^{-1}$ ^{103}Rh for In and Sn were used as internal standards. The dissolution in $\mu\text{g}_{\text{Pt}} \mu\text{g}_{\text{Pt}}^{-1}$ was determined via integration of the ICP-MS signal data by the flow rate (normalized to Pt mass loading on the GC electrode). The integration boundaries were taken from a constant signal area before and after the peak.

Supporting Information

Supporting Information is available from the Wiley Online Library or from the author.

Acknowledgements

This project received financial support from German Research Foundation (DFG) through grant STR 596/4-1 ("Pt-Stability") and the German Federal Ministry of Education and Research (BMBF) through grant 03SF0531B ("HT-linked"). M.H. and M.G. thank the DFG for financial support within the grant HE 7192/1-1. The authors thank ESRF and HZB Bessy II for allocation of synchrotron radiation beamtime and E. Hornberger and F. Dionigi for their help during beamtimes. ZELMI of Technical University Berlin is acknowledged for their support with TEM measurements. The authors thank A. Wittebrock for her help with electrochemical measurements.

Conflict of Interest

The authors declare no conflict of interest.

Keywords

catalyst degradation, in situ X-ray, nanoparticles, oxide supported platinum, oxygen reduction reaction

Received: June 17, 2017

Revised: August 4, 2017

Published online:

- [1] a) J. Speder, I. Spanos, A. Zana, J. J. Kirkensgaard, K. Mortensen, L. Altmann, M. Bäumer, M. Arenz, *Surf. Sci.* **2015**, *631*, 278; b) G. P. Keeley, S. Cherevko, K. J. J. Mayrhofer, *ChemElectroChem* **2016**, *3*, 51; c) C. Baldizzone, L. Gan, N. Hodnik, G. P. Keeley, A. Kostka, M. Heggen, P. Strasser, K. J. J. Mayrhofer, *ACS Catal.* **2015**, *5*, 5000; d) H. Yano, M. Watanabe, A. Iiyama, H. Uchida, *Nano Energy* **2016**, *29*, 323.
- [2] S. Cherevko, G. P. Keeley, S. Geiger, A. R. Zeradjanin, N. Hodnik, N. Kulyk, K. J. J. Mayrhofer, *ChemElectroChem* **2015**, *2*, 1471.
- [3] X. Tuae, S. Rudi, V. Petkov, A. Hoell, P. Strasser, *ACS Nano* **2013**, *7*, 5666.
- [4] a) C. A. Rice, P. Urchaga, A. O. Pistono, B. W. McFerrin, B. T. McComb, J. Hu, *J. Electrochem. Soc.* **2015**, *162*, F1175; b) F. Hasche, M. Oezaslan, P. Strasser, *J. Electrochem. Soc.* **2012**, *159*, B25; c) F. Hasche, M. Oezaslan, P. Strasser, *Phys. Chem. Chem. Phys.* **2010**, *12*, 15251; d) A. Riese, D. Banham, S. Ye, X. Sun, *J. Electrochem. Soc.* **2015**, *162*, F783; e) J. Speder, A. Zana, I. Spanos, J. J. K. Kirkensgaard, K. Mortensen, M. Hanzlik, M. Arenz, *J. Power Sources* **2014**, *261*, 14, f) L. Li, L. P. Hu, J. Li, Z. D. Wei, *Nano Res.* **2015**, *8*, 418.
- [5] Y. Luo, N. Alonso-Vante, *Electrochim. Acta* **2015**, *179*, 108.
- [6] a) V. R. Stamenkovic, B. Fowler, B. S. Mun, G. Wang, P. N. Ross, C. A. Lucas, N. M. Markovic, *Science* **2007**, *315*, 493; b) L. Gan, C. Cui, M. Heggen, F. Dionigi, S. Rudi, P. Strasser, *Science* **2014**, *346*, 1502; c) M. Escudero-Escribano, P. Malacrida, M. H. Hansen, U. G. Vej-Hansen, A. Velázquez-Palenzuela, V. Tripkovic, J. Schiötz, J. Rossmeisl, I. E. L. Stephens, I. Chorkendorff, *Science* **2016**, *352*, 73.
- [7] V. Beermann, M. Gocyla, E. Willinger, S. Rudi, M. Heggen, R. E. Dunin-Borkowski, M.-G. Willinger, P. Strasser, *Nano Lett.* **2016**, *16*, 1719.
- [8] a) Y. Shao, J. Liu, Y. Wang, Y. Lin, *J. Mater. Chem.* **2009**, *19*, 46; b) N. F. Zheng, G. D. Stucky, *J. Am. Chem. Soc.* **2006**, *128*, 14278.
- [9] S.-Y. Huang, P. Ganesan, S. Park, B. N. Popov, *J. Am. Chem. Soc.* **2009**, *131*, 13898.
- [10] A. Lewera, L. Timperman, A. Roguska, N. Alonso-Vante, *J. Phys. Chem. C* **2011**, *115*, 20153.
- [11] V. T. Ho, C. J. Pan, J. Rick, W. N. Su, B. J. Hwang, *J. Am. Chem. Soc.* **2011**, *133*, 11716.
- [12] A. Kumar, V. Ramani, *J. Electrochem. Soc.* **2013**, *160*, F1207.
- [13] A. Kumar, V. Ramani, *ACS Catal.* **2014**, *4*, 1516.
- [14] a) A. Kumar, V. K. Ramani, *Appl. Catal., B* **2013**, *138*, 43; b) C.-P. Lo, V. Ramani, *ACS Appl. Mater. Interfaces* **2012**, *4*, 6109; c) C.-P. Lo, G. Wang, A. Kumar, V. Ramani, *Appl. Catal., B* **2013**, *140*, 133; d) J. Parrondo, T. Han, E. Niangar, C. Wang, N. Dale, K. Adjemian, V. Ramani, *Proc. Natl. Acad. Sci. USA* **2014**, *111*, 45.
- [15] M. L. Dou, M. Hou, D. Liang, W. T. Lu, Z. G. Shao, B. L. Yi, *Electrochim. Acta* **2013**, *92*, 468.
- [16] T. Tsukatsune, Y. Takabatake, Z. Noda, T. Daio, A. Zaitso, S. M. Lyth, A. Hayashi, K. Sasaki, *J. Electrochem. Soc.* **2014**, *161*, F1208.
- [17] G. Cognard, G. Ozouf, C. Beauger, G. Berthomé, D. Riassetto, L. Dubau, R. Chattot, M. Chatenet, F. Maillard, *Appl. Catal., B* **2017**, *201*, 381.
- [18] a) Y. Liu, W. E. Mustain, *J. Am. Chem. Soc.* **2013**, *135*, 530; b) S. Zhao, A. E. Wangstrom, Y. Liu, W. A. Rigdon, W. E. Mustain, *Electrochim. Acta* **2015**, *157*, 175.
- [19] Y. Liu, W. E. Mustain, *Electrochim. Acta* **2014**, *115*, 116.
- [20] G. Wang, K. Bhattacharyya, J. Parrondo, V. Ramani, *Chem. Eng. Sci.* **2016**, *154*, 81.
- [21] a) A. Cuesta, A. Couto, A. Rincón, M. C. Pérez, A. López-Cudero, C. Gutiérrez, *J. Electroanal. Chem.* **2006**, *586*, 184; b) A. López-Cudero, A. Cuesta, C. Gutiérrez, *J. Electroanal. Chem.* **2006**, *586*, 204; c) F. Maillard, M. Eikerling, O. V. Cherstiouk, S. Schreiber, E. Savinova, U. Stimming, *Faraday Discuss.* **2004**, *125*, 357; d) D. F. van der Vliet, C. Wang, D. G. Li, A. P. Paulikas, J. Greeley, R. B. Rankin, D. Strmcnik, D. Tripkovic, N. M. Markovic, V. R. Stamenkovic, *Angew. Chem., Int. Ed.* **2012**, *51*, 3139.
- [22] S. Rudi, C. Cui, L. Gan, P. Strasser, *Electrocatalysis* **2014**, *5*, 408.
- [23] H. Borchert, E. V. Shevehenko, A. Robert, I. Mekis, A. Kornowski, G. Grubel, H. Weller, *Langmuir* **2005**, *21*, 1931.
- [24] S. Cherevko, A. R. Zeradjanin, G. P. Keeley, K. J. J. Mayrhofer, *J. Electrochem. Soc.* **2014**, *161*, H822.
- [25] W. Ostwald, *Z. Phys. Chem.* **1897**, *22*, 289.
- [26] L. Wang, F. Dionigi, N. T. Nguyen, R. Kirchgeorg, M. Gliech, S. Grigorescu, P. Strasser, P. Schmuki, *Chem. Mater.* **2015**, *27*, 2360.

- [27] a) U. Diebold, *Surf. Sci. Rep.* **2003**, *48*, 53; b) Q. Fu, T. Wagner, *Surf. Sci. Rep.* **2007**, *62*, 431; c) Q. Fu, T. Wagner, S. Olliges, H. D. Carstanjen, *J. Phys. Chem. B* **2005**, *109*, 944; d) V. A. O'Shea, M. C. Galvan, A. E. Prats, J. M. Campos-Martin, J. L. Fierro, *Chem. Commun. (Cambridge, U. K.)* **2011**, *47*, 7131; e) M. Yoshida, K. Takanabe, K. Maeda, A. Ishikawa, J. Kubota, Y. Sakata, Y. Ikezawa, K. Domen, *J. Phys. Chem. C* **2009**, *113*, 10151; f) S. Bonanni, K. Ait-Mansour, H. Brune, W. Harbich, *ACS Catal.* **2011**, *1*, 385; g) M. G. Willinger, W. Zhang, O. Bondarchuk, S. Shaikhutdinov, H. J. Freund, R. Schlögl, *Angew. Chem., Int. Ed.* **2014**, *53*, 5998; h) X. Y. Shi, W. Zhang, C. Zhang, W. T. Zheng, H. Chen, J. G. Qi, *J. Microsc. (Oxford, U. K.)* **2016**, *262*, 203; i) C. Spoeri, J. T. Kwan, A. Bonakdarpour, D. Wilkinson, P. Strasser, *Angew. Chem., Int. Ed. Engl.* **2016**, *56*, 5994; j) F. Micoud, F. Maillard, A. Bonnefont, N. Job, M. Chatenet, *Phys. Chem. Chem. Phys.* **2010**, *12*, 1182.
- [28] F. Dionigi, P. C. K. Vesborg, T. Pedersen, O. Hansen, S. Dahl, A. Xiong, K. Maeda, K. Domen, I. Chorkendorff, *J. Catal.* **2012**, *292*, 26.
- [29] R. Rizo, M. J. Lázaro, E. Pastor, M. T. M. Koper, *ChemElectroChem* **2016**, *3*, 2196.
- [30] K. Kakinuma, Y. Chino, Y. Senoo, M. Uchida, T. Kamino, H. Uchida, S. Deki, M. Watanabe, *Electrochim. Acta* **2013**, *110*, 316.
- [31] M. Nakada, A. Ishihara, S. Mitsushima, N. Kamiya, K. Ota, *Electrochem. Solid-State Lett.* **2007**, *10*, F1.
- [32] M. C. Santos, L. O. S. Bulhoes, *Electrochim. Acta* **2003**, *48*, 2607.
- [33] H.-S. Oh, H. N. Nong, T. Reier, A. Bergmann, M. Gliech, J. Ferreira de Araújo, E. Willinger, R. Schlögl, D. Teschner, P. Strasser, *J. Am. Chem. Soc.* **2016**, *138*, 12552.
- [34] G. N. Vayssilov, Y. Lykhach, A. Migani, T. Staudt, G. P. Petrova, N. Tsud, T. Skala, A. Bruix, F. Illas, K. C. Prince, V. Matolin, K. M. Neyman, J. Libuda, *Nat. Mater.* **2011**, *10*, 310.
- [35] S. Rudi, L. Gan, C. H. Cui, M. Gliech, P. Strasser, *J. Electrochem. Soc.* **2015**, *162*, F403.
- [36] A. Thust, J. Barthel, K. Tillmann, *J. Large Scale Res. Facil.* **2016**, *2*, A41.
- [37] A. Kovács, R. Schierholz, K. Tillmann, *J. Large Scale Res. Facil.* **2016**, *2*, A43.
- [38] a) S. Cherevko, A. R. Zeradjanin, A. A. Topalov, G. P. Keeley, K. J. J. Mayrhofer, *J. Electrochem. Soc.* **2014**, *161*, H501; b) A. K. Schuppert, A. A. Topalov, I. Katsounaros, S. O. Klemm, K. J. J. Mayrhofer, *J. Electrochem. Soc.* **2012**, *159*, F670.